Title: Small LEA proteins as an effective air-water interface protectant for fragile samples during cryo-EM grid plunge freezing

Authors: Kaitlyn M. Abe[1] & Ci Ji Lim[1,*]

Affiliations: [1]Department of Biochemistry, University of Wisconsin-Madison, Madison, WI 53706

[*]**Correspondence:** Ci Ji Lim

Email: ciji.lim@wisc.edu

Abstract

Sample loss due to air-water interface (AWI) interactions is a significant challenge during cryo-electron microscopy (cryo-EM) sample grid plunge freezing. We report that small Late Embryogenesis Abundant (LEA) proteins, which naturally bind to AWI, can protect samples from AWI damage during plunge freezing. This protection is demonstrated with two LEA proteins from nematodes and tardigrades, which rescued the cryo-EM structural determination outcome of two fragile multisubunit protein complexes.

Main

The 'resolution revolution' of cryogenic-electron microscopy (cryo-EM) marks a significant shift in the field of structural biology[1]. However, the continued growth of cryo-EM single particle analysis (SPA) structural biology faces an unexpected problem at the step of sample grid preparation — sample damage[1–4 1,5,6]. The standard method for cryo-EM SPA sample grid preparation is plunge freezing, where small volumes of sample are applied onto a pretreated cryo-EM grid, blotted, and rapidly plunge-frozen into a cryogen such as liquid ethane. This process forms a very thin layer (~50-100 nm) of sample-embedded vitreous ice for transmission electron microscopy imaging[7,8]. After the blotting and before the rapid freezing step, the sample exists as a thin aqueous film with a high surface-to-volume ratio. During this transitional phase (typically in seconds), the proteins in the aqueous solution collide with the air-water interface (AWI) multiple times before the sample hits the cryogen for vitrification. Adsorption to the AWI can destroy the protein's structural integrity, causing it to denature, or disintegrate[3,5,9,10] **(Fig. 1a).** In a scenario where the protein maintains its structure after AWI adsorption, the sample interaction with the AWI may be biased, leading to preferred sample orientations. A non-uniform representation of the protein along the imaging axis results in an anisotropic 3D reconstruction of the sample[1,10–12].

To mitigate the AWI problem, researchers have developed a variety of solutions. These include the addition of mild detergents to the sample[6], the use of chemical crosslinking[3,13,14], and adsorbing or tethering samples to surfaces to prevent sample contact with the AWI[12,15–24]. More sophisticated advanced techniques involve rapidly freezing the sample before the proteins can diffuse to the AWIs[25–27]. However, these methods are often sample-specific, technically challenging, or cost-prohibitive. In this study, we report a simple, effective, and economical approach for cryo-EM SPA users to circumvent issues related to AWI sample damage. In this work, we show that late embryogenesis abundant (LEA) proteins, which naturally bind to the AWI[28], can be utilized to shield samples from AWI-induced damage during cryo-EM grid plunge freezing (**Fig. 1a**). This new approach enables us to determine cryo-EM SPA structures of challenging multisubunit protein complexes at higher or comparable resolution than those previously reported using complicated AWI damage deterrent methods.

The AWI protective function of LEA proteins is demonstrated with proteins from two organisms: AavLEA1[28–31] from the nematode *Aphelenchus avenae* and RvLEAM[20] from the tardigrade *Ramazzottius varieornatus*, also known as water bears. These proteins are small — approximately 16 kilodaltons (kDa)

for AavLEA1 and 30 kDa for RvLEAM. Hence, we deduced that their small size enables rapid diffusion in solution, allowing them to reach the AWI faster than the larger protein samples of interest (typically, they are several hundred kDa in size). The LEA proteins will be stably adsorbed to the AWI due to their natural AWI affinity, thus forming a protective protein layer preventing the samples from contacting the AWI (**Fig. 1a**). In this study, RvLEAM was truncated (hereafter termed RvLEAM1$_{short}$) to approximately 15 kDa to further enhance diffusion efficiency (refer to the methods section for details).

To evaluate the AWI protective effects of the LEA proteins, we used two protein complexes that are AWI-sensitive as model systems: human DNA polymerase-α-primase (PP)[32–34] and Polycomb repressive complex-2 (PRC2)[35,36]. It is important to note that in this study, both complexes were tested in their apo-state, and all data collection was performed using a 200 keV electron microscope with a direct electron detector. Reported cryo-EM structures of apo-state PP complexes were solved using chemically crosslinked samples[34], suggesting that the PP particles fell apart due to AWI damage during plunge freezing. Indeed, in our hands, we saw no discernable PP particles using standard plunge freezing conditions with a Vitrobot (Mark IV, Thermo Fisher Scientific, USA) (**Fig. 1c**). Another arguably more challenging structure to solve for cryo-EM SPA is that of PRC2. Reported PRC2 cryo-EM structures were solved by highly specialized strategies using either chemically crosslinked samples on carbon-support grids[37,38] or biotinylated samples tethered onto Streptavidin-crystal grids[13,39–42].

We found that the addition of AavLEA1 or RvLEAM1$_{short}$ to PP and PRC2 prior to freezing eliminate the need for the abovementioned complicated methods, allowing us to solve their structures at comparable or higher cryo-EM map resolutions (**Fig. 1c-l**). The optimal range of addition is found to be between 1:6-1:40 molar ratio of the sample to the LEA proteins (**Extended Data Fig. 1**). For example, the addition of AavLEA1 at a 1:40 PP:AavLEA1 molar ratio before plunge freezing led to a much more positive outcome than the PP sample grid without any additives; we saw discernable and homogeneously sized particles (**Fig. 1c**). Multiple high-resolution two-dimensional (2D) class averages of PP were obtained from these particles (**Fig. 1d**). Subsequent image processing led to a 3.0 Å global resolution cryo-EM map of the apo-state PP (**Fig. 1e-g, and Extended Data Fig. 2**). This cryo-EM map is the highest resolution reported for the human apo-state PP; the previous X-ray structure was solved at 3.6 Å[43] and a chemically crosslinked cryo-EM structured determined at a 3.8 Å global resolution[34]. Most importantly, we demonstrated that LEA proteins, AavLEA1 in this case, can be used to "resuscitate" an unviable cryo-EM project and achieve high-resolution cryo-EM structures.

Initial concerns with the AavLEA1 strategy are 1) elevated background signal in the micrograph from the AavLEA1 addition and 2) AavLEA1 distorting the conformation of the sample of interest. In our experiments, we found no significant increase in the background signal (**Fig. 1c**), even at the highest tested AavLEA1:sample ratio of 40:1. If there were any, it did not affect image alignment or hindered high-resolution cryo-EM structure determination, as can be seen from our high-resolution map of PP (**Fig. 1g**). In addition, we did not find any extra map density that would indicate AavLEA1 binding to PP nor a significant change in the conformation (R.M.S.D of 1.1 Å when aligned to 5EXR[43], see **Extended Data Fig. 3**). In short, AavLEA1 addition did not alter PP apo-state conformation.

CHAPSO, a zwitterionic detergent, can protect protein samples from AWI damage during plunge freezing[44,45]. In our hands, it has been an effective strategy for determining the high-resolution cryo-EM structures of PP-related complexes[33,46]. Hence, we want to compare AavLEA1's efficiency in obtaining a high-resolution cryo-EM structure against CHAPSO. To this end we determined a 3.5 Å cryo-EM map of apo-state PP using CHAPSO (**Extended Data Fig. 4**). By visual inspection, we found no discernable differences between the two cryo-EM maps. Their particle image quality is also approximately similar, as indicated by ResLog analysis[47] (**Extended Fig. 5**). Thus, the particle quality in the AavLEA1 dataset is comparable to that of the CHAPSO dataset.

However, the use of CHAPSO or similar detergents requires a significantly higher concentration of samples[48] — over 4 mg/mL or approximately 13 µM for a 300 kDa protein sample. This presents a challenge for precious samples. In contrast, with AavLEA1, we only use around 1-1.5 µM of sample protein, which is more than ten times less than what is required for detergents. Therefore, AavLEA1 offers a valuable option when sample is limiting. In our hands, sample aggregation is a common problem from adding detergents. Another benefit of AavLEA1 is the early detection of potential interaction with the protein sample. If interaction occurs, it is more likely to be detected in a preliminary low-resolution cryo-EM map given AavLEA1's size of ~15 kDa. This is unlike CHAPSO, a small molecule that requires sub-4 Å resolution maps for detection[45].

We saw similar results for PRC2 with the addition of AavLEA1 (1:40 PRC2:AavLEA1 molar ratio) — Adding AavLEA1 resulted in discernable and homogeneously sized particles (**Fig. 1h**). Without additives, we saw smaller sized particles in the micrographs, indicating broken PRC2 complexes which is consistent as previously reported[13]. Subsequent cryo-EM image processing led to a 3.62 Å global resolution cryo-EM map of PRC2 (**Fig. 1i-l**). To our knowledge, this is the first high-resolution cryo-EM map of PRC2 that was obtained without the use of chemical crosslinking or adsorption to a carbon surface. This achievement further exemplifies the efficacy of AavLEA1 in facilitating the determination of high-resolution cryo-EM structures of protein samples sensitive to the air-water interface.

Notably, the AavLEA1-derived PRC2 cryo-EM map suffered from preferred particle orientation (**Fig. 1j & k**). In retrospect, the AavLEA1-derived PP cryo-EM map also has a certain degree of biased particle orientations, although this did not prevent us from obtaining an isotropic map (**compare Fig. 1g, and Extended Data Fig. 4**). If the LEA proteins are indeed providing protection to the protein samples from AWI interactions, one would expect the sample particles to exhibit a random yet evenly distributed orientation, like the one observed with the PP cryo-EM map in the presence of CHAPSO (**Extended Data Fig. 4c**). A possible explanation to why there is a biased but different particle orientation in the AavLEA1-PP and -PRC2 datasets is that the AavLEA1 protective layer at the AWI interacts with the protein samples in a manner specific to each sample. Nonetheless, these interactions do not appear to compromise the integrity of both samples, as evidenced by their high-resolution cryo-EM maps. In addition, problems associated with preferred particle orientation can be mitigated by employing tilted-stage data collection methods[11].

After establishing AavLEA1's efficacy in AWI protection, we investigated whether the tardigrade LEA protein, RvLEAM, exhibits similar protective qualities. Indeed, $RvLEAM_{short}$ similarly protects PP (**Extended Data Fig. 6**) and PRC2 (**Fig. 2a and Extended Data Fig. 7**) from AWI damage during plunge-freezing, suggesting that AWI protection is a universal characteristic of LEA proteins. We also noticed that the cryo-EM maps of PP and PRC2 obtained from the $RvLEAM_{short}$ datasets had particle orientation distributions comparable to those seen in the AavLEA1 datasets (**refer to Fig. 1j and 2a**). This similarity in particle orientation distribution between the two datasets suggests a shared AWI protection mechanism by the LEA proteins. Both AavLEA1 and $RvLEAM_{short}$ are predicted to form amphiphilic alpha helical structures, with the hydrophobic face oriented towards the air at the AWI and the hydrophilic side (negatively charged) facing the aqueous solution[49,50]. This offers a simple explanation for the observed similarity in particle orientation distributions when samples are exposed to either of the LEA proteins — both LEA proteins present a negatively-charged surface (water-facing) at the AWI.

Next, we explored conditions to improve PRC2 particle orientation distribution in the presence of $RvLEAM_{short}$ (**Fig. 2b-d**). First, we added divalent cation, $MgCl_2$, to attempt to neutralize the negatively charged surface presented by $RvLEAM_{short}$ at the AWI, with the hope that this strategy will change the PRC2 particle orientation distribution. Indeed, we observed a significant shift in the PRC2 particle orientation distribution, but the distribution is still heavily biased (**Fig. 2b**). Next, we crosslinked the

PRC2 samples with glutaraldehyde before freezing it with $RvLEAM_{short}$ (**Extended Data Fig. 8**). The carbonyl ends of glutaraldehyde form Schiff bases with the positively charged groups on the protein surface. This can neutralize the positively charged surface of PRC2 and change a sample's particle orientation distribution[51]. Indeed, we found additional new particle views in the crosslinked PRC2-$RvLEAM_{short}$ dataset and obtained a 3.10 Å cryo-EM map of PRC2 with improved isotropy (**Fig. 2c**). A milder crosslink treatment yielded a similar outcome (**Extended Data Fig. 9**). We also noticed significantly more intact PRC2 particles during image processing for these crosslinked datasets. The above suggests cryo-EM users can combine chemical crosslinking and LEA protein AWI protection for challenging cryo-EM samples.

Discussion

In summary, we showed that LEA proteins is an effective sample protectant for AWI damage in cryo-EM grid preparation. By simply adding AavLEA1 or $RvLEAM_{short}$ to samples before plunge freezing, we were able to determine the cryo-EM structures of both PP and PRC2 at comparable, or better resolution than those previously reported using more challenging and complicated anti-AWI damage strategies[13,34,37–42]. The LEA protein additives provide a simple, robust, and cost-effective anti-AWI damage solution that any cryo-EM labs and facilities in the world can readily incorporate into their existing workflow.

Figure legends

Figure 1. Nematode AavLEA1 effectively shields PP and PRC2 from AWI damage.

(a) Cartoon illustration of typical outcomes when protein samples (blue) interact with the air-water interface (AWI) before vitrification. AWI damage can lead to complete denaturation (left) or partial subunit dissociation (right). **(b)** Cartoon model of the proposed LEA protein sample protection mechanism. LEA proteins form a protective protein layer at AWI, preventing larger protein samples from interacting with the AWI. LEA proteins shown as grey α-helices and protein complexes in blue. The protected protein samples may be intact but adopt biased orientations (left), or evenly distributed (right) in ice. **(c)** Representative micrographs of human DNA polymerase-α-primase (PP) with no additives (top) or with AavLEA1 at 1:40 molar ratio (bottom). **(d)** Representative two-dimensional (2D) class averages of PP with AavLEA1 (1:40). **(e)** Particle orientation distribution analysis of the PP-AavLEA1 (1:40) cryo-EM map. **(f)** Fourier-shell correlation (FSC) curve of the PP-AavLEA1 (1:40) cryo-EM map. **(g)** Cryo-EM map of PP-AavLEA1 (1:40) with a global resolution of 3.0 Å (reported at 0.143 FSC). **(h)** Representative micrographs of human Polycomb Repressive Complex 2 (PRC2) without (top) or with AavLEA1 added at 1:40 molar ratio (bottom). **(i)** Representative 2D class averages of PRC2 with AavLEA1 (1:40). **(j)** Particle orientation distribution analysis of the PRC2-AavLEA1 (1:40) cryo-EM map. **(k)** FSC curve of the PRC2-AavLEA1 (1:40) cryo-EM map. **(l)** Cryo-EM map of PRC2-AavLEA1 (1:40) dataset with a global resolution of 3.8 Å.

Figure 2. Tardigrade RvLEAM$_{short}$ protects PRC2 from AWI damage and can be used in conjunction with other buffer additives to diversify particle orientation distribution.

(a) PRC2-RvLEAM$_{short}$ (1:6 molar ratio) cryo-EM single-particle analysis: representative micrograph, particle orientation analysis, FSC curve, and the cryo-EM map with a 3.6 Å global resolution. **(b)** PRC2-RvLEAM$_{short}$ (1:6 molar ratio) with 10 mM $MgCl_2$ cryo-EM single-particle analysis: representative micrograph, particle orientation analysis, FSC curve, and the cryo-EM map with a 4.2 Å global resolution. **(c)** PRC2-RvLEAM$_{short}$ (1:6 molar ratio) with 10 minutes of glutaraldehyde crosslinking cryo-EM single-particle analysis: representative micrograph, particle orientation analysis, FSC curve, and the cryo-EM map with a 3.1 Å global resolution. All global resolution values are reported at 0.143 FSC threshold.

185 **References**

186 1. Xu, Y. & Dang, S. Recent Technical Advances in Sample Preparation for Single-Particle Cryo-EM. *Front.*
187 *Mol. Biosci.* **9**, 892459 (2022).
188 2. Klebl, D. P. *et al.* Need for Speed: Examining Protein Behavior during CryoEM Grid Preparation at
189 Different Timescales. *Structure* **28**, 1238-1248.e4 (2020).
190 3. Glaeser, R. M. Proteins, interfaces, and cryo-EM grids. *Curr. Opin. Colloid Interface Sci.* **34**, 1–8 (2018).
191 4. Glaeser, R. M. & Han, B.-G. Opinion: hazards faced by macromolecules when confined to thin
192 aqueous films. *Biophys. Rep.* **3**, 1–7 (2017).
193 5. Noble, A. J. *et al.* Reducing effects of particle adsorption to the air–water interface in cryo-EM. *Nat.*
194 *Methods* **15**, 793–795 (2018).
195 6. Liu, N. & Wang, H.-W. Better Cryo-EM Specimen Preparation: How to Deal with the Air–Water
196 Interface? *J. Mol. Biol.* 167926 (2022) doi:10.1016/j.jmb.2022.167926.
197 7. Dubochet, J., Chang, J.-J., Freeman, R., Lepault, J. & McDowall, A. W. Frozen aqueous suspensions.
198 *Ultramicroscopy* **10**, 55–61 (1982).
199 8. Adrian, M., Dubochet, J., Lepault, J. & McDowall, A. W. Cryo-electron microscopy of viruses. *Nature*
200 **308**, 32–36 (1984).
201 9. Glaeser, R. M. Preparing Better Samples for Cryo–Electron Microscopy: Biochemical Challenges Do
202 Not End with Isolation and Purification. *Annu. Rev. Biochem.* **90**, 451–474 (2021).
203 10. Han, B.-G., Avila-Sakar, A., Remis, J. & Glaeser, R. M. Challenges in making ideal cryo-EM
204 samples. *Curr. Opin. Struct. Biol.* **81**, 102646 (2023).
205 11. Tan, Y. Z. *et al.* Addressing preferred specimen orientation in single-particle cryo-EM through
206 tilting. *Nat. Methods* **14**, 793–796 (2017).
207 12. D'Imprima, E. *et al.* Protein denaturation at the air-water interface and how to prevent it. *eLife* **8**,
208 e42747 (2019).

209 13. Lipscomb, D. M. Electron microscopy methods to overcome the challenges of structural
210 heterogeneity and preferred orientations in small (sub-500 kDa) macromolecular complexes.
211 (University of California, Berkeley, 2017).
212 14. Zhao, D. Y. *et al.* Cryo-EM structure of the native rhodopsin dimer in nanodiscs. *J. Biol. Chem.*
213 **294**, 14215–14230 (2019).
214 15. Wang, F. *et al.* General and robust covalently linked graphene oxide affinity grids for high-
215 resolution cryo-EM. *Proc. Natl. Acad. Sci.* **117**, 24269–24273 (2020).
216 16. Wang, F. *et al.* Amino and PEG-amino graphene oxide grids enrich and protect samples for high-
217 resolution single particle cryo-electron microscopy. *J. Struct. Biol.* **209**, 107437 (2020).
218 17. Wang, L. *et al.* Structure and mechanogating of the mammalian tactile channel PIEZO2. *Nature*
219 **573**, 225–229 (2019).
220 18. Liu, N. *et al.* Bioactive Functionalized Monolayer Graphene for High-Resolution Cryo-Electron
221 Microscopy. *J. Am. Chem. Soc.* **141**, 4016–4025 (2019).
222 19. Glaeser, R. M. & Han, B.-G. Streptavidin Affinity Grids for Single-particle Cryo-EM. *Microsc.*
223 *Microanal.* **25**, 990–991 (2019).
224 20. Cookis, T. *et al.* Streptavidin-Affinity Grid Fabrication for Cryo-Electron Microscopy Sample
225 Preparation. *J. Vis. Exp.* 66197 (2023) doi:10.3791/66197.
226 21. Palovcak, E. *et al.* A simple and robust procedure for preparing graphene-oxide cryo-EM grids. *J.*
227 *Struct. Biol.* **204**, 80–84 (2018).
228 22. Lu, Y. *et al.* Functionalized graphene grids with various charges for single-particle cryo-EM. *Nat.*
229 *Commun.* **13**, 6718 (2022).
230 23. Zheng, L. *et al.* Uniform thin ice on ultraflat graphene for high-resolution cryo-EM. *Nat. Methods*
231 **20**, 123–130 (2023).

232 24. Han, Y. *et al.* High-yield monolayer graphene grids for near-atomic resolution cryoelectron
233 microscopy. *Proc. Natl. Acad. Sci.* **117**, 1009–1014 (2020).
234 25. Jain, T., Sheehan, P., Crum, J., Carragher, B. & Potter, C. S. Spotiton: A prototype for an
235 integrated inkjet dispense and vitrification system for cryo-TEM. *J. Struct. Biol.* **179**, 68–75 (2012).
236 26. Rubinstein, J. L. *et al.* Shake-it-off: a simple ultrasonic cryo-EM specimen-preparation device.
237 *Acta Crystallogr. Sect. Struct. Biol.* **75**, 1063–1070 (2019).
238 27. Tan, Y. Z. & Rubinstein, J. L. Through-grid wicking enables high-speed cryoEM specimen
239 preparation. *Acta Crystallogr. Sect. Struct. Biol.* **76**, 1092–1103 (2020).
240 28. Yuen, F. *et al.* Preferential adsorption to air–water interfaces: a novel cryoprotective mechanism
241 for LEA proteins. *Biochem. J.* **476**, 1121–1135 (2019).
242 29. Chakrabortee, S. *et al.* Intrinsically disordered proteins as molecular shields. *Mol BioSyst* **8**, 210–
243 219 (2012).
244 30. Tunnacliffe, A. & Wise, M. J. The continuing conundrum of the LEA proteins.
245 *Naturwissenschaften* **94**, 791–812 (2007).
246 31. Hincha, D. K. & Thalhammer, A. LEA proteins: IDPs with versatile functions in cellular
247 dehydration tolerance. *Biochem. Soc. Trans.* **40**, 1000–1003 (2012).
248 32. He, Q. & Lim, C. J. Models for human telomere C-strand fill-in by CST–Polα-primase. *Trends*
249 *Biochem. Sci.* **48**, 860–872 (2023).
250 33. He, Q. *et al.* Structures of human primosome elongation complexes. *Nat. Struct. Mol. Biol.* **30**,
251 579–583 (2023).
252 34. Kilkenny, M. L. *et al.* Structural basis for the interaction of SARS-CoV -2 virulence factor nsp1
253 with DNA polymerase α–primase. *Protein Sci.* **31**, 333–344 (2022).
254 35. Ciferri, C. *et al.* Molecular architecture of human polycomb repressive complex 2. *eLife* **1**,
255 e00005 (2012).

256 36. Davidovich, C., Zheng, L., Goodrich, K. J. & Cech, T. R. Promiscuous RNA binding by Polycomb
257 repressive complex 2. *Nat. Struct. Mol. Biol.* **20**, 1250–1257 (2013).
258 37. Kasinath, V. *et al.* Structures of human PRC2 with its cofactors AEBP2 and JARID2. *Science* **359**,
259 940–944 (2018).
260 38. Grau, D. *et al.* Structures of monomeric and dimeric PRC2:EZH1 reveal flexible modules involved
261 in chromatin compaction. *Nat. Commun.* **12**, 714 (2021).
262 39. Kasinath, V. *et al.* JARID2 and AEBP2 regulate PRC2 in the presence of H2AK119ub1 and other
263 histone modifications. *Science* **371**, eabc3393 (2021).
264 40. Song, J. *et al.* Structural basis for inactivation of PRC2 by G-quadruplex RNA. *Science* **381**, 1331–
265 1337 (2023).
266 41. Hemphill, W. O., Fenske, R., Gooding, A. R. & Cech, T. R. PRC2 direct transfer from G-quadruplex
267 RNA to dsDNA has implications for RNA-binding chromatin modifiers. *Proc. Natl. Acad. Sci.* **120**,
268 e2220528120 (2023).
269 42. Poepsel, S., Kasinath, V. & Nogales, E. Cryo-EM structures of PRC2 simultaneously engaged with
270 two functionally distinct nucleosomes. *Nat. Struct. Mol. Biol.* **25**, 154–162 (2018).
271 43. Baranovskiy, A. G. *et al.* Mechanism of Concerted RNA-DNA Primer Synthesis by the Human
272 Primosome. *J. Biol. Chem.* **291**, 10006–10020 (2016).
273 44. Chen, S., Li, J., Vinothkumar, K. R. & Henderson, R. Interaction of human erythrocyte catalase
274 with air – water interface in cryoEM. *Microscopy* **71**, i51–i59 (2022).
275 45. Chen, J., Noble, A. J., Kang, J. Y. & Darst, S. A. Eliminating effects of particle adsorption to the
276 air/water interface in single-particle cryo-electron microscopy: Bacterial RNA polymerase and
277 CHAPSO. *J. Struct. Biol. X* **1**, 100005 (2019).
278 46. He, Q. *et al.* Structures of the human CST-Polα–primase complex bound to telomere templates.
279 *Nature* **608**, 826–832 (2022).

280 47. Stagg, S. M., Noble, A. J., Spilman, M. & Chapman, M. S. ResLog plots as an empirical metric of
281 the quality of cryo-EM reconstructions. *J. Struct. Biol.* **185**, 418–426 (2014).
282 48. Snijder, J. *et al.* Vitrification after multiple rounds of sample application and blotting improves
283 particle density on cryo-electron microscopy grids. *J. Struct. Biol.* **198**, 38–42 (2017).
284 49. Tanaka, S. *et al.* Novel Mitochondria-Targeted Heat-Soluble Proteins Identified in the
285 Anhydrobiotic Tardigrade Improve Osmotic Tolerance of Human Cells. *PLOS ONE* **10**, e0118272 (2015).
286 50. Li, D. & He, X. Desiccation Dependent Structure and Stability of an Anhydrobiotic Nematode Late
287 Embryogenesis Abundant (LEA) Protein. in *ASME 2009 Summer Bioengineering Conference, Parts A*
288 *and B* 213–214 (American Society of Mechanical Engineers, Lake Tahoe, California, USA, 2009).
289 doi:10.1115/SBC2009-206862.
290 51. Stark, H. GraFix: Stabilization of Fragile Macromolecular Complexes for Single Particle Cryo-EM.
291 in *Methods in Enzymology* vol. 481 109–126 (Elsevier, 2010).
292
293

294 **Methods**

295 **Expression and purification of AavLEA1 and RvLEAM$_{short}$**

296 The expression plasmid for HIS-tagged AavLEA1 was obtained from the Addgene plasmid repository
297 [pET15b-AavLEA1 was a gift from Claude Férec (Addgene plasmid # 53093)][52] The expression plasmid for
298 HIS-tagged RvLEAM$_{short}$ was made by inserting a truncated cDNA from pEThT-RvLEAM[49] [pEThT-RvLEAM
299 was a gift from Takekazu Kunieda (Addgene plasmid # 90033)], into the pET15b vector. RvLEAM$_{short}$
300 encodes residues 58-181 of RvLEAM (A0A0E4AVP3.1). Recombinant AavLEA1 and RvLEAM$_{short}$ were
301 expressed in *Escherichia coli* BL21 (DE3) cells. Briefly, a single bacterial colony with the transformed
302 plasmid was inoculated in 2 mL Luria Bertani broth (LB) with 100 µg mL^{-1} carbenicillin and grown
303 overnight at 37°C. This starter culture was then used to inoculate 1 L of LB supplemented with
304 antibiotics. Once the culture reached an absorbance (A_{600}) of 0.6, gene expression was induced with 0.1
305 mM isopropyl-β-D-thiogalactopyranoside (IPTG) for 16 hours at 12°C, shaking at 230 rpm.

306 Next morning, the cells were harvested by centrifugation and resuspended in lysis buffer (50 mM HEPES
307 pH 7.5, 300 mM NaCl, 10 mM imidazole, 1 mM DTT/TCEP, 1 mM PMSF). The cells were lyzed by
308 sonication and then centrifuged to remove debris. Pre-equilibrated nickel-NTA resin (Qiagen, 50 mg/mL
309 binding capacity) was added to the clarified lysate and the lysate-resin slurry stirred in a beaker with a
310 stir bar for 1 hour at 4°C. The protein-bound resin was washed three times, each time using 50 mL of
311 lysis buffer. After the final wash, 10 mL of elution buffer (wash buffer supplemented with final 250 mM
312 imidazole) was added to the resin, and the eluted protein collected using a gravity flow column. The
313 proteins were concentrated to ~500 uL using a 3 kDa MWCO spin column before it is injected into a
314 Superdex 75 10/300 size-exclusion chromatography (SEC) column (Cytiva, USA) that is pre-equilibrated
315 with SEC buffer (50 mM HEPES pH 7.5, 300 mM NaCl, 1 mM DTT/TCEP, 10% glycerol). Eluted fractions
316 were collected and analyzed by SDS-PAGE. Fractions containing the proteins were pooled, concentrated
317 and then snap-frozen as 5-10 µL aliquots. The frozen aliquots are stored in a -80°C freeze until usage.

318 **Production of recombinant human DNA Polymerase alpha-primase and Polycomb repressive complex**
319 **2**

320 Recombinant human DNA Polymerase alpha-primase were expressed in insect cells using baculovirus
321 infection and purified as previously reported[46]. Purified recombinant human PRC2 protein complexes
322 were generous gifts from Dr. Thomas Cech at the University of Colorado Boulder. The expression and
323 purification protocols of PRC2 has be described previously[40].

324 **PRC2 glutaraldehyde crosslinking**

325 Approximately 2 µM PRC2 were incubated with a 0.1% (v/v) final glutaraldehyde concentration for 2-
326 and 10-minute time intervals. After each interval, an aliquot is removed and quenched with 80 mM Tris-
327 HCl to stop the reaction. SDS-PAGE was used to determine the crosslinking efficiency of the PRC2
328 samples at various incubation time point.

329 **Cryo-EM sample grid preparation and plunge-freezing**

330 All samples used were thawed just prior to cryo-EM grid preparation. Holey carbon cryo-EM grids, either
331 Quantifoil R 1.2/1.3 300 mesh Au or C-flat R 1.2/1.3 300 mesh Au were glow discharged on a PELCO
332 EasiGlow glow-discharge unit (15 mA for 30 seconds with 10 second hold). The protein samples were

333 diluted to working concentration right before grid application in 25 mM HEPES pH 7.5, 150 mM NaCl, 1
334 mM TCEP. Where indicated, buffer was supplemented with CHAPSO or $MgCl_2$. Then 3.5 µL of the
335 sample was applied to the glow discharged grid. The grid was then blotted for 4 to 6 seconds at 4°C and
336 95% humidity, and then plunge frozen into liquid ethane using a Vitrobot Mark IV (Thermo Fisher, USA).

337 For all conditions except those specified, 1 – 1.5 µM of PP or PRC2 were used with the indicated molar
338 ratio of AavLEA1 or $RvLEAM_{short}$. For conditions using PP and 4 mM CHAPSO, 13.8 µM PP was used.

339 **Cryo-EM data collection**

340 All data collections and screening were done on a Talos Arctica 200 kV TEM (Thermo Fisher, USA) with a
341 Gatan BioQuantum K3 direct electron detector (Gatan, USA). Data screening and acquisition software
342 used was either EPU (Thermo Fisher, USA) or SerialEM[53]. All cryo-EM datasets were collected at a pixel
343 size of 1.064 Å/pixel with a total dose of 50 $e^{-}Å^{-2}$ across 40 frames. CDS counting mode was used with
344 energy filter inserted at 20 eV. Defocus range used was -1 to -2.5 µm.

345 **Cryo-EM data processing**

346 For all datasets, image processing was performed using cryoSPARC[54]. Briefly, movies were motion
347 corrected and the ensuing micrographs had their contrast transfer function (CTF) estimated. The CTF
348 values were used to curate a set of micrographs that are suitable for high-resolution single-particle
349 analysis. Details of subsequent image processing steps for each dataset are as follows:

350

351 <u>1.5 µM PP, 12 µM AavLEA1 (1:8) dataset</u>

352 A total of 2,764 movies were collected. After micrograph curation 2,112 movies remained and 1,724,984
353 particles were extracted at 4x binning (4.3 Å per pixel). After 2D classification, 785,653 particles
354 proceeded to ab-initio reconstruction and sorted into four separated reference-free 3D classes. Particles
355 underwent another round of ab-initio modeling and separated into two classes. The intact complex was
356 sorted into one of the two classes (239,029 particles, 75%) and non-uniform refinement of this class
357 with per-particle CTF refinement resulted in a global resolution (reported at Fourier shell correlation of
358 0.143) of 3.6 Å.

359 <u>1.5 µM PP, 60 µM AavLEA1 (1:40) dataset</u>

360 A total of 4,403 movies were collected. After micrograph curation, 500 movies were initially used with a
361 total of 340,430 particles extracted at 4x binning. From 2D classification, 201,337 particles were selected
362 and re-extracted at original pixel size. Particles then proceeded to ab-initio reconstruction and were
363 sorted into four separated reference-free 3D classes. Two of the four classes resulted in intact particles,
364 which were verified through non-uniform refinement of the combined classes using 165,472 particles,
365 resulting in a 3.8 Å structure. Particles were extracted from the remaining 3,771 movies and binned 4x,
366 resulting in 2,668,602 particles. These particles were then sorted into 2D classes, and the selected
367 1,438,074 particles underwent ab-initio modeling. Selected particles underwent another round of ab-
368 initio modeling with two classes. One of the two classes showed intact particles, and those 1,009,026
369 particles were sent to non-uniform refinement yielding a 3.43 Å global resolution. CryoSparc global and
370 local CTF refinement jobs were run followed by further filtering, resulting in 988,417 particles. These
371 particles were then extracted at the original pixel size. All resulting particles underwent non-uniform

372 refinement, reference motion correction, and heterogeneous refinement. 856,205 particles were used
373 for a final non-uniform refinement, with a final global resolution of 3.0 Å.

374 The published apo-state PP (PDB: 5EXR)[43] model was used as the initial model for real space refinement
375 against the cryo-EM map using the Phenix software[55]. Structural alignment between the 5EXR model
376 and the refined model was performed using the matchmaker module in the ChimeraX software[56]. The
377 refinement statistics and validation report are available in Supplementary Table 1.

378 1 μM PP, 6 μM RvLEAM$_{short}$ (1:6) dataset

379 A total of 1,308 movies were collected. Following micrograph curation, 335,907 particles were extracted
380 from 1,076 micrographs and binned 4x. 125,231 particles were extracted with 2D classification. These
381 particles then proceeded to ab-initio reconstruction and split into 3D classes. The selected 74,198
382 particles were re-extracted at the original pixel size from 1,071 micrographs. Particles underwent
383 another round of 2D classification and Ab-Initio 3D reconstruction. Selected particles underwent non-
384 uniform refinement and had a final global resolution of 4.5 Å. The final resolution of this dataset is lower
385 than our other PP datasets which is likely because this data collection contains only 1,308 movies while
386 other PP datasets had 2,700 or more movies.

387 13.8 μM PP, 4 mM CHAPSO dataset

388 A total of 4,567 movies were collected. Following micrograph curation, 1,832,455 particles were
389 extracted from 4,510 micrographs and binned 4x. Particles underwent 2D classification where and ab-
390 initio reconstruction. Selected particles were used to re-extract at the original pixel size (744,824
391 particles). Extracted particles were then sorted into 2D classes underwent non-uniform refinement with
392 per-particle CTF refinement and reference motion correction, with a final global resolution of 3.4 Å with
393 674,793 particles.

394 1.5 μM PRC2, 60 μM AavLEA1 (1:40) dataset

395 A total of 2,843 movies were collected. Following micrograph curation, 687,121 particles were extracted
396 from 1,642 micrographs and binned 4x. Particles underwent 2D classification and ab-initio
397 reconstruction. Selected classes were re-extracted at original pixel size, yielding 150,359 particles. The
398 re-extracted particles underwent non-uniform refinement with per-particle CTF refinement and resulted
399 in a global resolution of 3.8 Å.

400 1 μM PRC2, 12 μM AavLEA1 (1:12) dataset

401 A total for 4,356 movies were collected. Following micrograph curation, 2,073,578 particles were
402 extracted from 4,112 movies and binned 4x. Particles were sorted into 2D classes followed by ab-Initio
403 3D classes. One of the four classes showed an intact complex, so the 275,416 particles from this class
404 were re-extracted at the original pixel size from 4,110 movies. Re-extracted particles underwent another
405 round of ab-initio 3D reconstruction. The final 238,045 particles underwent non-uniform refinement,
406 with a final global resolution of 3.7 Å.

407 1 μM PRC2, 6.7 μM RvLEAM$_{short}$ (~1:6) dataset

408 A total of 3,896 movies were collected. Following micrograph curation, 1,766,944 particles were
409 extracted from 3,637 micrographs and binned 4x. Particles were sorted into 2D classes followed by 3D

classes via ab-Initio reconstruction. The selected 547,610 particles were re-extracted and subjected to ab-initio 3D reconstruction. The final 206,807 particles underwent non-uniform refinement with per-particle CTF refinement, resulting in a global resolution of 3.8 Å.

1 µM PRC2, 6.7 µM RvLEAM$_{short}$ (~1:6) 10 mM $MgCl_2$ dataset

A total of 4,333 movies were collected. Following micrograph curation, 1,755,138 particles were extracted from 3,759 micrographs and binned 4x. Particles underwent two rounds of 2D classification From here, 408,373 particles were selected and proceeded to ab-initio 3D reconstruction. The resulting 406,148 particles were re-extracted from 3,746 movies at the original pixel size and underwent another round of ab-initio reconstruction. The final 102,181 particles proceeded to non-uniform refinement with a final global resolution was 4.2 Å.

1 µM PRC2 cross-linked 2 minutes, 6.7 µM RvLEAM$_{short}$ (~1:6) dataset

A total of 2,981 movies were collected. Following micrograph curation, 982,264 particles were extracted from 2,189 movies and binned 4x. Particles were sorted into 2D classes followed by 3D classes via ab-initio reconstruction. Selected particles were re-extracted at the original pixel size and underwent ab-initio reconstruction again. The resulting 654,585 particles were subjected to non-uniform refinement with per-particle CTF refinement, resulting in a global resolution of 3.5 Å.

1 µM PRC2 cross-linked 10 minutes, 6.7 µM RvLEAM$_{short}$ (~1:6) dataset

A total of 3,432 movies were collected. Following micrograph curation, 2,084,816 particles were extracted from 3,295 movies and binned 4x. Particles underwent 2D classification followed by ab-initio 3D reconstruction. Selected particles were re-extracted at the original pixel size. Particles underwent non-uniform refinement, resulting in a global resolution of 3.3 Å. Global CTF refinement, reference-based motion correction and heterogeneous refinement jobs were run. 366,459 particles were used in this final round of non-uniform refinement, resulting in a global resolution of 3.1 Å.

434 **Methods references**

435 52. Tripathi, R., Benz, N., Culleton, B., Trouvé, P. & Férec, C. Biophysical Characterisation of

436 Calumenin as a Charged F508del-CFTR Folding Modulator. *PLoS ONE* **9**, e104970 (2014).

437 53. Mastronarde, D. N. Automated electron microscope tomography using robust prediction of

438 specimen movements. *J. Struct. Biol.* **152**, 36–51 (2005).

439 54. Punjani, A., Rubinstein, J. L., Fleet, D. J. & Brubaker, M. A. cryoSPARC: algorithms for rapid

440 unsupervised cryo-EM structure determination. *Nat. Methods* **14**, 290–296 (2017).

441 55. Adams, P. D. *et al. PHENIX*: a comprehensive Python-based system for macromolecular

442 structure solution. *Acta Crystallogr. D Biol. Crystallogr.* **66**, 213–221 (2010).

443 56. Meng, E. C. *et al.* UCSF CHIMERAX: Tools for structure building and analysis. *Protein Sci.* **32**,

444 e4792 (2023).

445

446

447

448

449

450

451

452

453

454 **Data availability**

455 The described cryo-EM maps and coordinate files have been deposited in the Electron Microscopy Data
456 Bank and the Protein Data Bank (PDB) under the accession codes: EMD-43619 (PP - AavLEA1, 1:8 molar
457 ratio), PDB-ID 8VY3 with EMD-43628 (PP - AavLEA1, 1:40 molar ratio), EMD-43626 (PP – $RvLEAM_{short}$, 1:6
458 molar ratio), EMD-43627 (PP – CHAPSO 4 mM), EMD-43620 (PRC2 – AavELA1, 1:40 molar ratio), EMD-
459 43621 (PRC2 – $RvLEAM_{short}$, 1:6 molar ratio), EMD-43622 (PRC2 – $RvLEAM_{short}$, 1:6 molar ratio, 10 mM
460 $MgCl_2$), EMD-43623 (PRC2 – AavLEA1, 1:12 molar ratio), EMD-43623 (PRC2 – $RvLEAM_{short}$, 1:6 molar ratio,
461 2 min cross-link), EMD-43625 (PRC2 – $RvLEAM_{short}$, 1:6 molar ratio, 10 min cross-link).

462 **Competing interests**

463 A provisional patent has been filed for this technology with the Wisconsin Alumni Research Foundation
464 (WARF).

465 **Author contributions**

466 C.L conceived the study. K.M.A. made the recombinant proteins, cryo-EM grids, performed data
467 collection and image processing with C.L. in support. K.M.A performed the crosslinking experiments and
468 analysis. K.M.A. and C.L. wrote the manuscript, with the figures made by K.M.A.

469 **Acknowledgments**

470 We thank Thomas Cech, Anne Gooding, and Jiarui Song at the University of Colorado Boulder for their
471 generous gift of purified recombinant human PRC2. We also thank Qixiang He, Xiuhua Lin, and the rest
472 of the Lim laboratory for their helpful suggestion and generous support of reagents. We thank Timothy
473 Grant and Elizabeth Wright for their helpful suggestions. Some of this work was performed in the Cryo-
474 EM Research Center (CEMRC) in the Department of Biochemistry at the University of Wisconsin-
475 Madison. We thank the staff at CEMRC for their support and assistance in cryo-EM data collection.
476 Support for this research was provided to C.L. by the National Institutes of Health (NIH), the National
477 Institute of General Medical Sciences (R00GM131023 and DP2GM150023) and the University of
478 Wisconsin–Madison, Office of the Vice-Chancellor for Research and Graduate Education with funding
479 from the Wisconsin Alumni Research Foundation and the Department of Biochemistry. In addition,
480 K.M.A is supported by a NIH T32 predoctoral fellowship (T32GM130550).

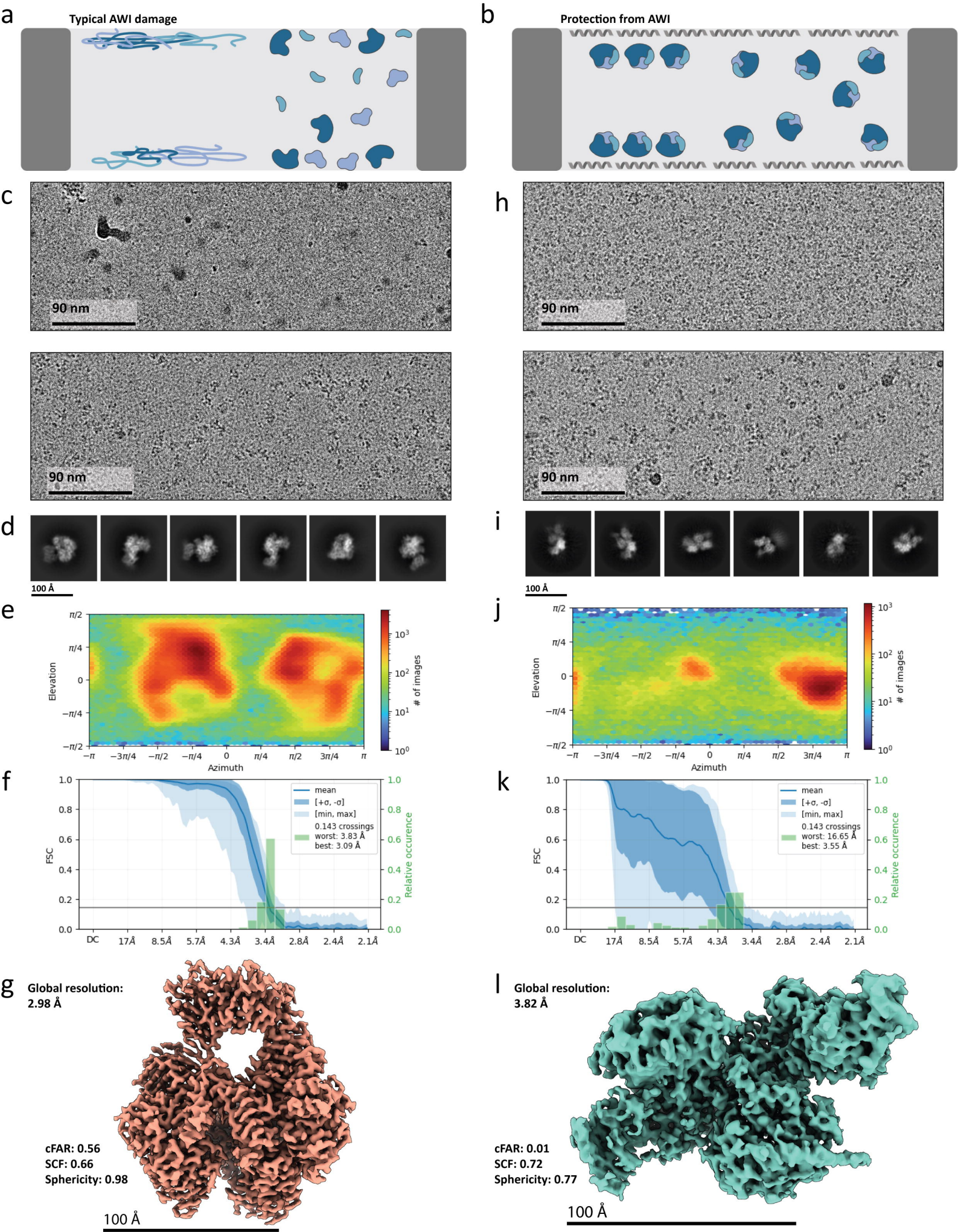
a
Typical AWI damage
b
Protection from AWI
c
90 nm
90 nm
h
90 nm
90 nm
d
100 Å
i
100 Å
e
Elevation
Azimuth
# of images
j
Elevation
Azimuth
# of images
f
FSC
Relative occurence
mean
[+σ, -σ]
[min, max]
0.143 crossings
worst: 3.83 Å
best: 3.09 Å
DC
17Å
8.5Å
5.7Å
4.3Å
3.4Å
2.8Å
2.4Å
2.1Å
k
FSC
Relative occurence
mean
[+σ, -σ]
[min, max]
0.143 crossings
worst: 16.65 Å
best: 3.55 Å
g
Global resolution:
2.98 Å
cFAR: 0.56
SCF: 0.66
Sphericity: 0.98
100 Å
l
Global resolution:
3.82 Å
cFAR: 0.01
SCF: 0.72
Sphericity: 0.77
100 Å

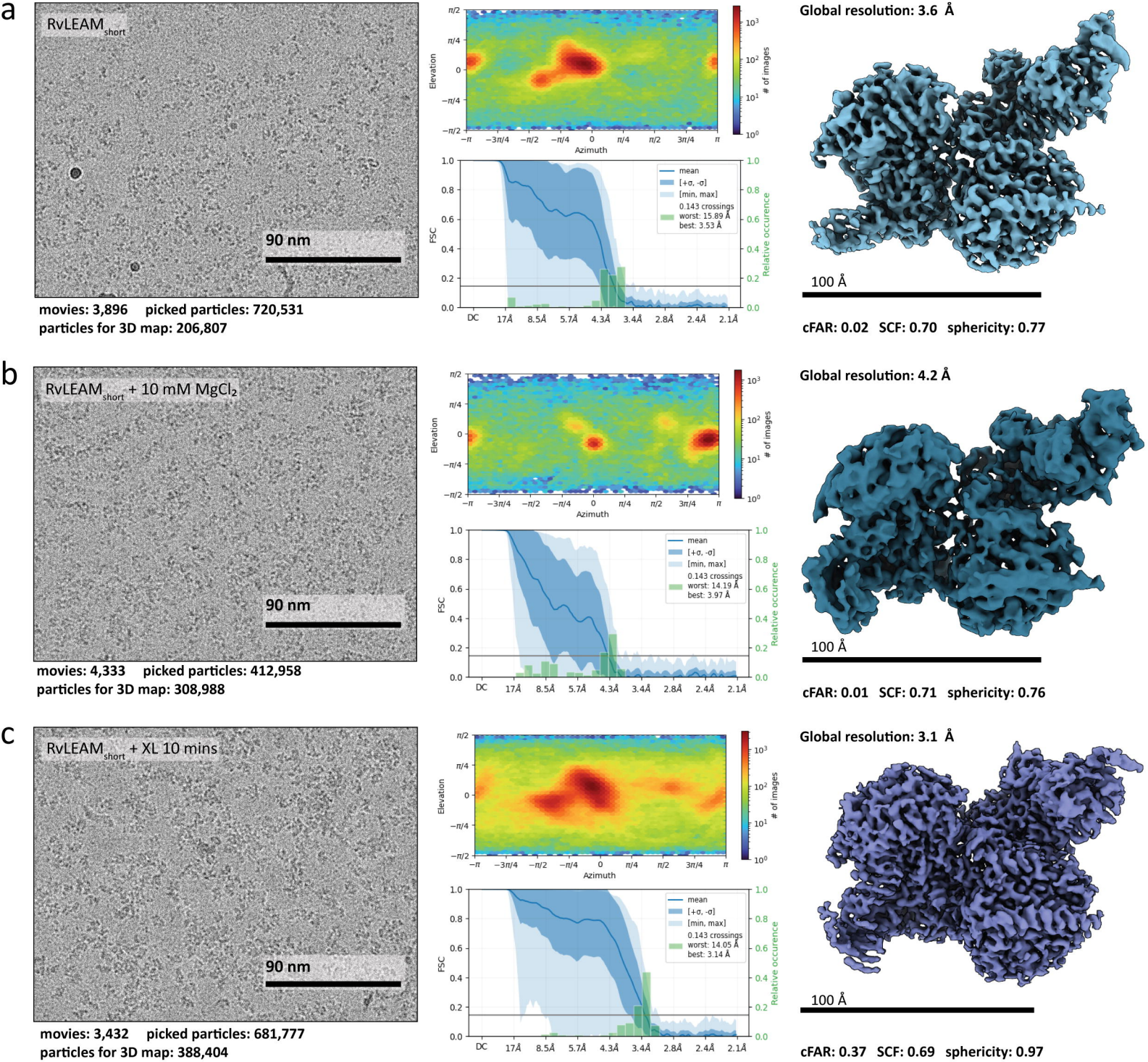
a
RvLEAM short
90 nm
movies: 3,896 picked particles: 720,531
particles for 3D map: 206,807
Elevation
Azimuth
# of images
FSC
Relative occurence
mean
[+σ, -σ]
[min, max]
0.143 crossings
worst: 15.89 Å
best: 3.53 Å
Global resolution: 3.6 Å
100 Å
cFAR: 0.02 SCF: 0.70 sphericity: 0.77
b
RvLEAM short + 10 mM MgCl2
90 nm
movies: 4,333 picked particles: 412,958
particles for 3D map: 308,988
worst: 14.19 Å
best: 3.97 Å
Global resolution: 4.2 Å
100 Å
cFAR: 0.01 SCF: 0.71 sphericity: 0.76
c
RvLEAM short + XL 10 mins
90 nm
movies: 3,432 picked particles: 681,777
particles for 3D map: 388,404
worst: 14.05 Å
best: 3.14 Å
Global resolution: 3.1 Å
100 Å
cFAR: 0.37 SCF: 0.69 sphericity: 0.97